# Hephaestus Minicubes: A Global, Multi-Modal Dataset for Volcanic Activity Monitoring

Nikolas Papadopoulos <sup>1</sup> npapadopoulos@mail.ntua.gr

Nikolaos Ioannis Bountos<sup>1,2</sup> bountos@noa.gr

Maria Sdraka<sup>1,2</sup> masdra@noa.gr

Andreas Karavias<sup>1</sup> andreas\_karavias@mail.ntua.gr

Ioannis Papoutsis<sup>1</sup>
ipapoutsis@mail.ntua.gr

Orion Lab National Observatory of Athens & National Technical University of Athens

<sup>2</sup> Harokopio University of Athens

## Supplemental material

## 2 A Detailed Dataset Description

- 3 This section details the annotation schema used in Hephaestus Minicubes. Building upon the expert
- 4 labels from the original *Hephaestus* dataset [Bountos et al., 2022], annotations were adapted to a
- 5 spatiotemporal format compatible with the datacube structure. A comprehensive view of the dataset
- variables can be seen in Tab. 1 and examples of different annotation types are shown in A.1. In the
- following paragraphs we will detail the key variables of *Hephaestus Minicubes*.
- 8 Activity. Activity-related segmentation masks lie at the core of the dataset's annotation schema
- 9 detailing the presence of deformation, its geophysical source and its intensity.
- 10 A high-level Deformation Mask, delineates Volcanic and Earthquake induced deformation pat-
- 11 terns.
- 12 The Activity Type Mask captures more detailed geophysical context, distinguishing among several
- common deformation source models: Mogi [Kiyoo, 1958], Dyke [Okada, 1985, Sigmundsson et al.,
- 14 2010], Sill [Fialko et al., 2001], and Spheroid [Yang et al., 1988], as well as deformation attributed
- to Earthquake events or labeled as Unidentified when no clear model can be observed.
- The Intensity Level Mask categorizes the strength of deformation signals based on the number of
- 17 visible fringes in the interferogram: Low (1 fringe), Medium (2-3 fringes), and High (more than
- 18 3 fringes). For earthquake-related events, the intensity is marked as None, reflecting their distinct
- 19 deformation characteristics.
- 20 Additionally, we include a *Phase* categorical variable that captures the state of the volcano *i.e.* Rest
- 21 (no sign of volcanic activity), Unrest (indicating uplift), or Rebound (indicating subsidence). Again,
- for Earthquake events, we set the phase to None.
- 23 Noise. A separate set of annotation variables aim to capture specific signal characteristics and
- 24 noise patterns. These include: glacier fringes, when observed fringes result from glacier melting
- (1 if present, 0 otherwise); orbital fringes, for phase ramps caused by satellite orbital errors; and
- atmospheric fringes, which take four values: type 0 (no atmospheric impact), type 1 (vertical

Table 1: Overview of Hephaestus Minicubes Dataset Variables

Variable	Description		
InSAR Products			
Phase Difference	Difference in SAR signal phase, indicating surface displacement.		
Coherence	The reliability of the interferometric phase measurement.		
Topography			
DEM	Digital Elevation Model: a representation of Earth's surface topography.		
Atmospheric Variables			
Total Column Water Vapour	Water vapour from surface to the top of the atmosphere.		
Surface Pressure	Atmospheric pressure at Earth's surface.		
Vertical Integral of Temperature	Mass-weighted temperature integral from surface to top of the atmo-		
	sphere.		
Annotations			
Deformation Mask	High level mask for deformation presence {Non-Deformation,		
	Volcanic, Earthquake}.		
Activity Type Mask	Mask identifying the activity type: {Sill, Dyke, Mogi, Spheroid,		
	Earthquake, Unidentified }.		
Intensity Level Mask	Mask identifying the intensity level of the activity {None, Low,		
	Medium, High}.		
Phase	Phase of the activity: {Rest, Unrest, Rebound, None }.		
Atmospheric Fringes	Identifies types of atmospheric noise.		
Glacier Fringes	Identifies deformation patterns from glacier melting.		
Orbital Fringes	Identifies phase ramps due to orbital errors.		
Corrupted	Flag for corrupted data.		
No Info	Identifies low-coherence interferograms, where meaningful interpreta-		
	tion is not possible.		
Low Coherence	Identifies samples that are characterized from interferometric signal		
	decorrelation.		
Is Crowd	Identifies whether multiple deformation masks exist.		
Caption	Expert text description of the interferogram and annotation rationale.		
Confidence	Value indicating the annotator's confidence [0-1].		
Metadata			
Unique Id	Unique identifier for each sample.		
Valid Date Pair	Boolean flag for primary/secondary dates with existing InSAR products.		

stratification correlated with topography due to changes in the troposphere's refractive index), type 2 (turbulent mixing and vapors caused by liquid or solid particles in the atmosphere), and type 3 (a combination of type 1 and type 2). The low coherence variable is set to 1 when interferometric 29 signal decorrelation dominates the image. No info is used when coherence is so low throughout the 30 interferogram that meaningful interpretation is not possible. 31

InSAR Processing Errors. Automated InSAR generation pipelines may, occasionally, result in 32 faulty products. To identify corrupted InSAR, and facilitate automatic detection of such instances in 33 future applications, we include a set of annotation variables denoting technical faults. The first is the 34 binary variable *corrupted*, which identifies interferograms that are entirely problematic and unusable. 35 The second is *processing error*, which distinguishes between specific InSAR processing errors: type 36 1 refers to debursting errors during the synchronization of bursts from one or more sub-swaths; type 37 2 indicates Sentinel-1 sub-swath merging errors, which appear as visible discontinuities, while type 38 0 denotes interferograms free of such processing issues. 39

**Meta-Information.** The *confidence* score is a continuous value in the range [0, 1] that reflects 40 the annotator's confidence regarding the deformation classification. The is crowd variable is set to 0 when at most one local fringe pattern is present and 1 when two or more such patterns appear within 42 the same interferogram. Furthermore, the caption field contains a text description providing expert 43 commentary, interpretation rationale, or relevant contextual notes for the InSAR phase difference product. Finally the unique id serves as a unique identifier for each sample, and the valid date pair 45 flag indicates whether the combination of primary and secondary dates corresponds to an existing 46 InSAR product, intended for use in the multi-dimensional array functionality.

41

**Annotation Process.** The annotation process was carried out by a team of InSAR experts through photo-interpretation on the available wrapped interferograms. Each image was optically inspected over the locations of volcanoes, as well as the surrounding areas, in order to evaluate the quality of the interferograms and indicate the impact of atmospheric delays and potential artifacts. Each

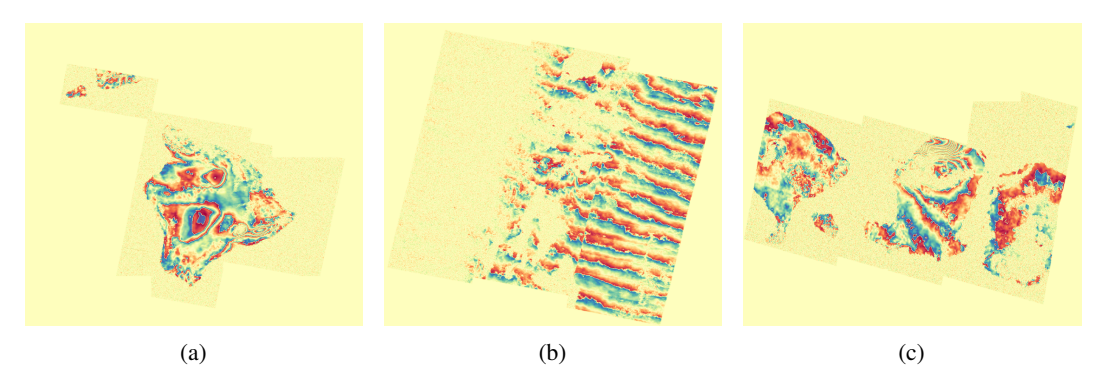
positive annotation was cross-validated via external sources (publications, reliable news sources) as well as the COMET Volcano Deformation Portal <sup>1</sup>, to support the evaluation of whether the observed displacement was due to true volcanic activity or atmospheric delay effects. For further details regarding the annotation process readers are referred to the original *Hephaestus* dataset [Bountos et al., 2022].

#### A.1 Visualizing Annotation Diversity

57

In this section we present selected examples of different annotation variables, illustrating the diversity and richness of the annotation variables in *Hephaestus Minicubes*.

Text Captions. In Fig. 1, we showcase InSAR imagery with various apparent deformation patterns and atmospheric phenomena, together with the expert textual captions, highlighting the complexity and variability captured in the dataset. Each caption provides a thorough description of the location and type of all underlying phenomena, as well as a reference to interpretation challenges if present.



- (a) "Vertical stratification can be detected on the high altitude areas. Turbulent mixing effect can also be detected on the right, central and top-left side. Two deformation patterns can be detected on the right side. A dyke-type of high intensity on the leftmost and sill-type of medium intensity on the rightmost."
- (b) "Turbulent mixing effect or wave-like patterns caused by liquid and solid particles of the atmosphere can be detected around the area. No deformation activity can be detected. Orbital fringes detected. Difficulties in extracting information."
- (c) "Noise can be detected on the bottom-right area. Turbulent mixing effect can be detected on the wider left and central side of the region. Vertical stratification can also be detected on the central-top side of the region. An earthquake deformation pattern can be detected on the top-central side of the region."

Figure 1: Textual annotations highlighting volcanic and atmospheric phenomena in InSAR imagery from the *Hephaestus Minicubes* dataset.

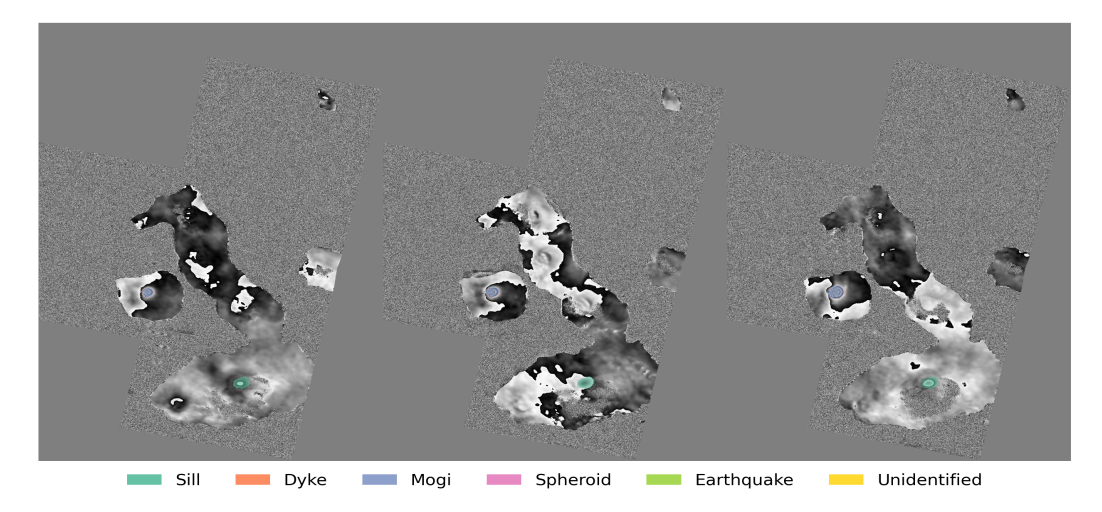
Activity and Intensity Masks. In Fig. 2, we present different time-series of InSAR products overlaid with expert-provided *activity type* and *intensity level* masks. These examples illustrate the temporal evolution of deformation signals and how distinct geophysical phenomena are annotated both categorically and in terms of intensity, emphasizing the structured labeling within *Hephaestus Minicubes*. The InSAR products are shown in grayscale for visual clarity.

## **B** Extended Experimental Details

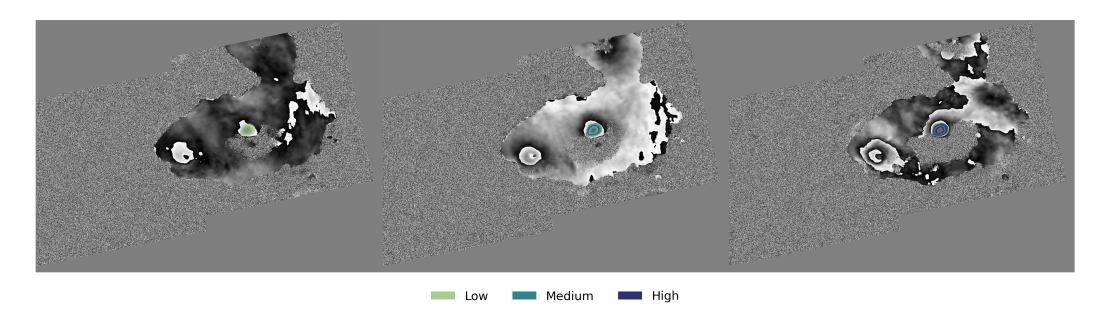
In this section we provide additional details on the experimental configurations used in the provided benchmark.

Time-series Construction. We construct the time-series by first grouping samples based on their primary SAR acquisition date. The distribution of the length of the resulting time-series can be seen in Fig. 3. Based on this, we fix the time-series length to 3, to ensure input consistency. For primary SAR acquisitions that produce time-series with length greater than 3, we extract all possible sub-sequences of the predefined length. Conversely, if they contain fewer than 3, we randomly duplicate available interferograms to reach the required time-series length.

https://comet.nerc.ac.uk/comet-volcano-portal/



(a) Overlay of activity type masks on a time-series of InSAR phase difference products.



(b) Overlay of intensity level masks on a time-series of InSAR phase difference products.

Figure 2: Examples of annotated InSAR products with overlayed annotated masks indicating: (a) distinct geophysical activity types and (b) activity intensity levels.

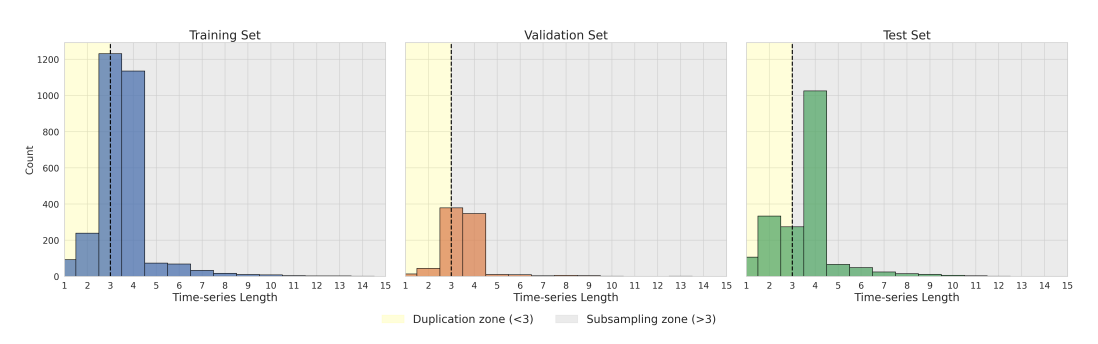


Figure 3: Distribution of time-series lengths across training, validation, and test sets.

78

81

82

83

84

85

**Training Setup.** We conducted all experiments on a single GPU (NVIDIA GeForce RTX 3090 Ti). We trained all models for 90 epochs, using the AdamW optimizer [Loshchilov and Hutter, 2017] with a fixed learning rate of  $10^{-5}$  and a weight decay set to  $10^{-2}$ . For classification, we found that cross-entropy loss consistently delivered the best performance, except for ViT that displayed more stable convergence with focal loss. For segmentation, focal loss was more effective, likely due to its robustness to class imbalance in pixel-wise annotations [Lin et al., 2017]. To mitigate the effect of class imbalance, we employed an undersampling strategy during training. For each epoch, all available positive samples were included, along with a randomly selected subset of negative samples of equal size. All models were trained with a random set of data augmentations including gaussian blur, random resize crop, horizontal and vertical flips and random rotations. Tables 2 and 3 report the

number of trainable parameters for all models along with the average runtime of each experiment for both classification and segmentation tasks respectively.

Table 2: Overview of classification architectures

	# Trainable parameters (M)		# Average runtime (hours)	
Model architecture	Single-image	Time-series	Single-image	Time-series
ResNet-50	23.5	23.6	2.2	2.7
MobileNetV3 (Large)	4.2	4.2	1.7	2.0
EfficientNetV2 (Small)	20.2	20.2	2.6	2.7
ConvNeXt (Small)	87.6	87.6	4.9	5.4
ViT (Small)	22.3	24.0	2.5	3.2

Table 3: Overview of segmentation architectures

		# Trainable parameters (M)		# Average runtime (hours)	
Model architecture	Backbone	Single-image	Time-series	Single-image	Time-series
DeepLabV3	ResNet-50	26.7	26.8	2.3	2.9
UNet	ResNet-50	32.5	32.6	2.3	3.0
SegFormer	ResNet-50	24.9	24.9	1.6	3.7

## **OCC** Qualitative Results and Model Insights

In this section, we present indicative examples that provide insights on models' performance beyond quantitative metrics, especially given the inherent ambiguities and complexities of the data.

Ambiguity in Segmentation Masks. As discussed in section 5 of the main text, delineating the exact boundaries of deformation is often ambiguous, especially in regions of high-incoherence. Such noise is inherent to the data itself, making the annotation, and thereby accurate prediction challenging. In Fig. 4 we offer two representative examples of qualitatively good model predictions that do not perfectly align with the annotator's estimation, indicating the aforementioned ambiguity. In this case, model predictions accurately identify the observable deformation patterns to some extent, but exclude the noisy areas. The human annotator, however, includes these noisy regions, considering them as part of the event, even if they do not exhibit ground deformation fringes.

**Time-Series Predictions.** Fig. 5 illustrates important insights concerning model predictions on time-series inputs. Although both time-series of the figure focus on the same volcanic region, variations in the spatial extent or deformation onset across time-steps can affect detection ability. In the first sequence, less-pronounced deformation patterns are only visible in the final time-step, which the model fails to detect. In contrast, the second sequence displays a progressively intensifying deformation signal starting from the second time-step, providing stronger temporal cues that allow the model to correctly identify and segment the affected area. This example highlights how both the timing and strength of deformation signals across the time-series could play an important role in the the model's ability to identify deformation.

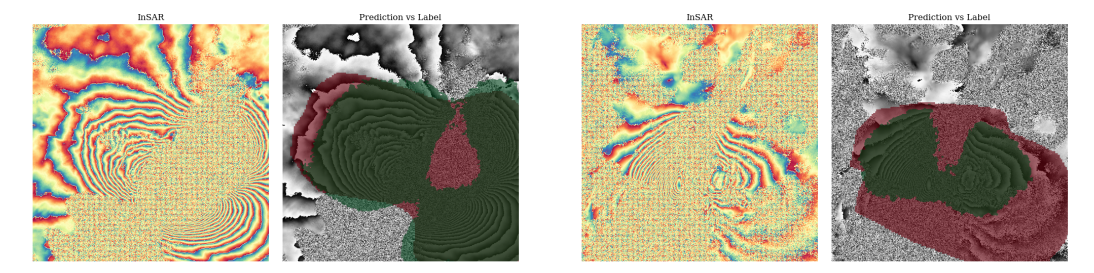


Figure 4: Qualitative examples of true positive model predictions that illustrate the inherent ambiguity in segmentation masks, where deformation extent is difficult to define. The left image of each pair depicts the InSAR phase difference, while the right image overlays the ground truth mask (in red) and the model prediction (in green) on the InSAR product (in grayscale). The results presented here have been obtained by the best performing DeepLabV3 model, which utilizes atmospheric data as input.

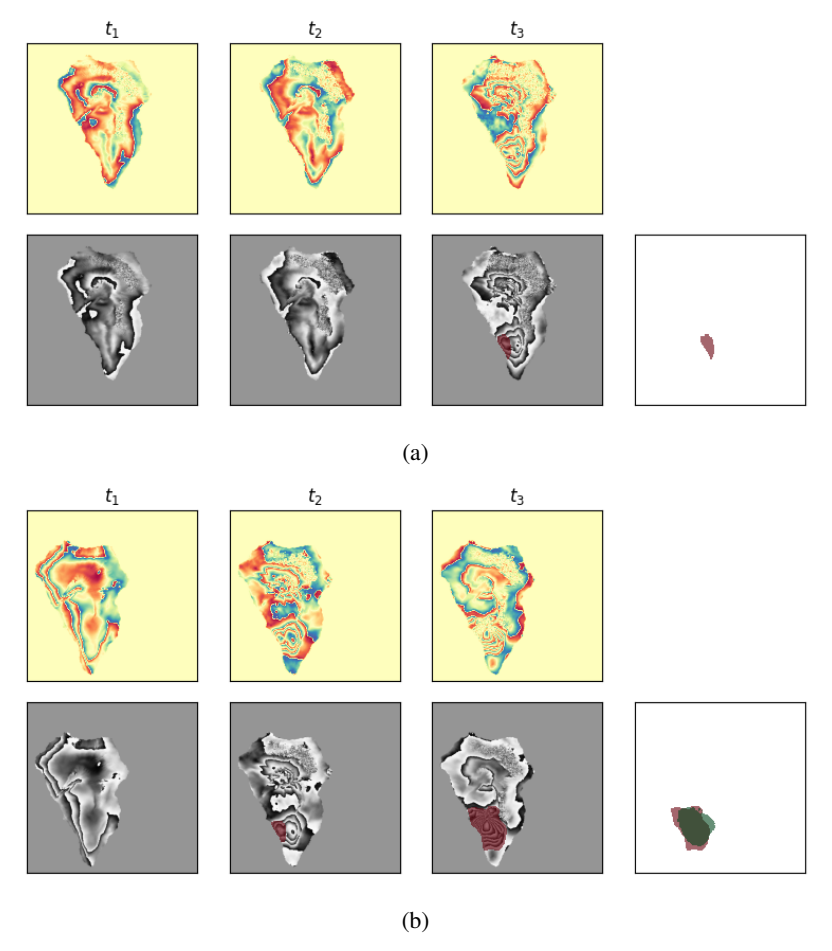


Figure 5: Time-series examples over La Palma, Tenerife, demonstrating the role of temporal context in model predictions. The upper image series of each subfigure depicts the InSAR products in each timestep, and the lower image series depicts the ground truth masks (in red) for each time step with the corresponding InSAR in grayscale as the background. The last image in the lower series depicts the union of all ground truth masks (in red) and the model predictions (in green). Results have been obtained with the best performing SegFormer model (with atmospheric input). Subfigure a) shows a false negative case where only the final time-step exhibits deformation, which the model fails to detect, while subfigure b) illustrates a case where the model successfully identifies the deformation due to its increased presence in the last two time-steps. These examples highlight how variations in signal strength and onset time can influence model prediction.

### o References

- Nikolaos Ioannis Bountos, Ioannis Papoutsis, Dimitrios Michail, Andreas Karavias, Panagiotis Elias, and Isaak Parcharidis. Hephaestus: A Large Scale Multitask Dataset Towards InSAR Understanding. In *Proceedings of the IEEE/CVF Conference on Computer Vision and Pattern* Recognition (CVPR) Workshops, pages 1453–1462, June 2022.
- Yuri Fialko, Yakov Khazan, and Mark Simons. Deformation due to a pressurized horizontal circular crack in an elastic half-space, with applications to volcano geodesy. *Geophysical Journal International*, 146(1):181–190, 2001.
- MOGI Kiyoo. Relations between the eruptions of various volcanoes and the deformations of the ground surfaces around them. *Earthq Res Inst*, 36(99):e134, 1958.
- Tsung-Yi Lin, Priya Goyal, Ross Girshick, Kaiming He, and Piotr Dollár. Focal loss for dense object detection. In *Proceedings of the IEEE international conference on computer vision*, pages 2980–2988, 2017.
- 123 Ilya Loshchilov and Frank Hutter. Decoupled weight decay regularization. *arXiv preprint* 124 *arXiv:1711.05101*, 2017.
- Yoshimitsu Okada. Surface deformation due to shear and tensile faults in a half-space. *Bulletin of the* seismological society of America, 75(4):1135–1154, 1985.
- Freysteinn Sigmundsson, Sigrún Hreinsdóttir, Andrew Hooper, Thóra Arnadóttir, Rikke Pedersen,
  Matthew J Roberts, Níels Óskarsson, Amandine Auriac, Judicael Decriem, Páll Einarsson, et al.
  Intrusion triggering of the 2010 eyjafjallajökull explosive eruption. *Nature*, 468(7322):426–430,
  2010.
- Xue-Min Yang, Paul M Davis, and James H Dieterich. Deformation from inflation of a dipping finite
   prolate spheroid in an elastic half-space as a model for volcanic stressing. *Journal of Geophysical Research: Solid Earth*, 93(B5):4249–4257, 1988.